Applied Geochemistry 176 (2024) 106208

Contents lists available at ScienceDirect

Applied Geochemistry

journal homepage: www.elsevier.com/locate/apgeochem

Trace element partitioning between natural barite and deep anoxic groundwaters: Implications for radionuclide retention in host rocks of nuclear waste repositories

Ferdinand Kirchner [a,*], Martin Kutzschbach [a], Henrik Drake [b], Vanessa Fichtner [b], Piotr M. Kowalski [c,d], Stefan Rudin [e], Martin J. Whitehouse [f], Mikael Tillberg [b], Thomas Neumann [a]

[a] Technische Universität Berlin, Department of Applied Geochemistry, 10587, Berlin, Germany
[b] Department of Biology and Environmental Science, Linnaeus University, 39231, Kalmar, Sweden
[c] Institute of Energy Technologies (IET-3) - Theory and Computation of Energy Materials, Forschungszentrum Jülich GmbH, Jülich, 52425, Germany
[d] Jülich Aachen Research Alliance, JARA Energy & Center for Simulation and Data Science (CSD), 52425, Jülich, Germany
[e] Institute of Fusion Energy and Nuclear Waste Management (IFN-2) - Nuclear Waste Management, Forschungszentrum Jülich GmbH, Jülich, 52425, Germany
[f] Laboratory for Isotope Geology, Swedish Museum of Natural History, Box 50007, SE-104 05, Stockholm, Sweden

ARTICLE INFO

Editorial handling by: Dr Mavrik Zavarin

Keywords:
Barite
Radionuclides
Nuclear waste repository
Partition coefficient
Radium
Actinides
LA-ICP-MS

ABSTRACT

Safety assessments for deep geological repositories involve risk calculations for the release of radionuclides like Ra, U, Pu and trivalent actinides from the storage containers to the groundwater. The retention of radionuclides through water-mineral interaction along the groundwater flow path could be a crucial factor in case of a repository failure. Barite ($BaSO_4$) assumes significance in this context, as it has the potential to (re)crystallize and incorporate significant quantities of radioactive elements under relevant physico-chemical conditions.

The assessment of mineral-fluid partition coefficients provides a means to evaluate the uptake potential of elements into the mineral. Usually, partition coefficients are determined under well-defined and controlled experimental conditions in laboratories. However, these results have shown discrepancies to partitioning coefficients determined from natural systems.

Furthermore, effects like diagenesis or changes in the chemical fluid parameters might lead to a secondary alteration of the phases and affecting the retention ability.

Here we investigate the incorporation of trace elements in natural barite from a borehole at 415 m depth in the Äspö Hard Rock Laboratory (Sweden). High-resolution LA-ICP-MS enables the quantitative determination of field-based partition coefficients through the integrated pixel average of selected zones in element distribution maps, combined with existing fluid concentration data. Similarities between the solid solution systems (Ra,Ba)SO_4 and (Sr,Ba)SO_4 allowed the combination of Sr partitioning data with density-functional theory simulations for an estimation of the partition coefficient value for Ra in natural barite. Values in the 10^{-2} range were determined, showing a deviation from those reported in previous experimental studies in the 10^{0} range.

Moreover, lanthanum serves as an analogue element for the radioactive trivalent actinides. The partition coefficient values for La in natural barite were determined in the range of 10^{-2} and 10^{-1}, aligning well with experimental partition coefficients. Although density functional theory simulations cannot directly convert a La partition coefficient into a partition coefficient for trivalent actinides, it is assumed that these elements exhibit comparable behavior. Besides primary growth zonation, La also exhibits strong secondary enrichment, probably resulting from groundwater mixing and late fluid-mediated element transport through connected intracrystalline pore space oriented at cleavage plane systems. Additional SIMS analysis provides insights into the temporal variation of the sulfate source at the sampling site reflecting the influence of different waters during mineral growth.

* Corresponding author.
E-mail address: kirchner@tu-berlin.de (F. Kirchner).

https://doi.org/10.1016/j.apgeochem.2024.106208
Received 4 January 2024; Received in revised form 16 October 2024; Accepted 25 October 2024
Available online 28 October 2024

This study demonstrates a discrepancy between natural and synthetic P_{Ra} for barite and emphasizes that secondary processes significantly impact radionuclide retention in barite. Including these effects in reactive transport models will improve the reliability and applicability of integrative risk models.

1. Introduction

The environmental issues related to operation of nuclear power plants and the accompanied production of high-level radioactive waste needs an adequate solution of long-term disposal. Currently, disposal in an underground repository in deep geological formations is considered the safest option (e.g., Kim et al., 2011; Birkholzer et al., 2012; Kurniawan et al., 2021). In searching for a suitable repository site, risks, which lead to a leakage of the waste canisters, shall be minimized as far as possible, for as long as possible. Modern repository sites are designed with a multi-barrier system (Olszewska et al., 2015; Apted and Ahn, 2017) aimed at prolonging the impact of waste corrosion for the maximum duration. However, within the necessary time frames for repository considerations, the potential for migration and release of radionuclides into the environment cannot be ruled out.

^{226}Ra is particularly significant among radionuclides due to its natural occurrence, which can lead to the accumulation of radioactivity in both natural systems and industrial facilities. Technologically enhanced naturally occurring radioactive material (TENORM) can cause issues in oil production, geothermal energy utilization, and groundwater desalination (Hamlat et al., 2003; IAEA, 2003; Rosenberg et al., 2013; Heberling et al., 2018). These TENORM and other radium-enriched materials, such as medical waste (Manocchi et al., 2014), must be disposed of as radioactive waste. Additionally, uranium mill tailings have elevated concentrations of ^{226}Ra, which can lead to a contamination of the groundwater system. In the long-term evolution of spent nuclear fuel, a secular equilibrium of ^{226}Ra with its parent nuclide ^{238}U will be reached, contributing to the radiation dose of potentially released material (SKB Technical Report TR-21-07, 2022). Additionally, trivalent actinides like Am or Cm are a long-lasting environmental risk as these are predominant residues of the PUREX process, which involves the extraction of Pu and U from spent fuels (Dares et al., 2015; Xiao et al., 2017).

Former studies have shown that barite can act as a scavenger for Ra in geological systems due to recrystallization of existing barite (Torapava et al., 2014; Brandt et al., 2015, 2020; Klinkenberg et al., 2018; Weber et al., 2017) or precipitation from the solution (Curti et al., 2010; Zielinski et al., 2010; Heberling et al., 2018).

To estimate the uptake potential of an element into a crystal, partition coefficients (P_{Me}; Me = metal), also known as distribution coefficients, have been determined in experiments resembling geological conditions in regions of a potential repository (Curti, 1999). However, these artificial conditions may not accurately resemble crystal growth in complex natural systems. Most obviously there is a discrepancy between the timescales at which experiments are typically conducted to deliver data in a reasonable amount of time (e.g., days to month) vs. the envisaged safety timescale for nuclear repository sites (e.g., 1 Ma in Germany). By comparing lab-based to natural fluid-calcite partition coefficients, Drake et al. (2018) noticed closely matching values for certain elements (e.g., Mg, Fe, Sr). However, notable discrepancies were evident for other elements such as Ba, Y, Yb, and REE.

These discrepancies encourage to determine the radionuclide partitioning behavior of natural systems to augment the input database for a comprehensive safety assessment modelling of potential long-term nuclear waste repositories.

As radioactive elements like Ra usually occur in traces in natural aquatic systems, their direct determination in barite by an in-situ analytical tool is difficult (Klinkenberg et al., 2014; Weber et al., 2017). Nevertheless, spatially resolved analysis is crucial to account for the complex growth history and associated zoning patterns in natural crystals over geological time scales. Therefore, the potential of radionuclide retention in natural minerals is commonly evaluated with the help of elements, which are assumed to behave similar to their radioactive equivalents regarding their chemical properties. Krauskopf (1986) described the rare earth elements (REE) as suitable analogues for the actinides Am and Cm, as they can only exist in the trivalent state (under typical repository conditions) and stability constants for their dissolved species and complexes are very similar to the REE. In this study, a potential uptake of trivalent actinides, like Am and Cm, into barite will be evaluated through the distribution of La, which is known to behave similar regarding incorporation (Seaborg, 1992; Drake et al., 2018). Probably the most well-suited analogue element to Ra is Sr because of the same ionic charge and its affiliation to the alkaline earth group metals, although some differences in chemical behavior have been documented (Zhang et al., 2014; Vinograd et al., 2018a, 2018b; Brandt et al., 2020).

In this study, recently formed barite samples and the surrounding groundwater from boreholes in the Swedish Nuclear Fuel and Waste Management Co. (SKB) operated Hard Rock Laboratory (HRL) in deep granitoid rock (>400 m below sea level) was investigated. This offers a unique opportunity to assess in situ metal uptake into barite under repository conditions within deep granitoid aquifers.

To quantify the concentrations of the relevant trace elements, LA-ICP-MS is a suitable technique as it enables in situ probing of solids with detection limits in the sub-ppm range (Durant and Ward, 2005). Depending on the laser spot size and ablation depth conventional LA-ICP-MS spot analysis may lead to misinterpretation of the calculated P_{Me} due to the mixed analyses of different growth zones. Nevertheless, reducing the laser spot size and utilizing a LA-ICP-MS configuration offering low-aerosol dispersion enables the mapping of trace elements with micrometer-scale resolution and exceptional sensitivity (van Acker et al., 2021; Pidchenko et al., 2023; Kutzschbach and Glodny, 2024). In this study high-resolution LA-ICP-MS mappings are combined with conventional LA-ICP-MS spot analysis to validate the mapping method.

By means of DFT simulations and using the assumed analogy of Sr for Ra, this contribution provides the first (to the best of our knowledge) reliable estimate of the Ra partition coefficients between barite and fluid in a natural deep anoxic aquifer. Moreover, valuable insights into barite's potential as a sink for trivalent actinides are deduced from the distribution of La.

2. Material and methods

2.1. Sampling of natural barite and fluids at Äspö Hard Rock Laboratory

The SKB operates a full-scale test facility in SE Sweden (Äspö HRL) in which two boreholes (A: KA3105A/at −415 m depth and B: KA3385A/at −445 m depth, from here on A and B, respectively) were drilled horizontally between 1994 and 1995 (Fig. 1a). Borehole A has a length of 52.01 m and borehole B 34.18 m. The boreholes accommodate an Al-rod and are separated by inflatable packers into discrete isolated (packer-) sections (Fig. 1b). Each of these sections is supplied by water from individual fractures that intersect the boreholes. The unique feature about this experiment is that the section-water was sampled through a polyamide tubing system which was attached to the Al-rod. The hydrostatic pressure in the borehole directs the water into sampling containers (individually for each section) without the need of a pump. Two distinct water types were collected for analysis: stagnant water, representing the resident water within the section, and fracture water, obtained after 10 discharges of the section volume. Fracture water is indicative of pristine

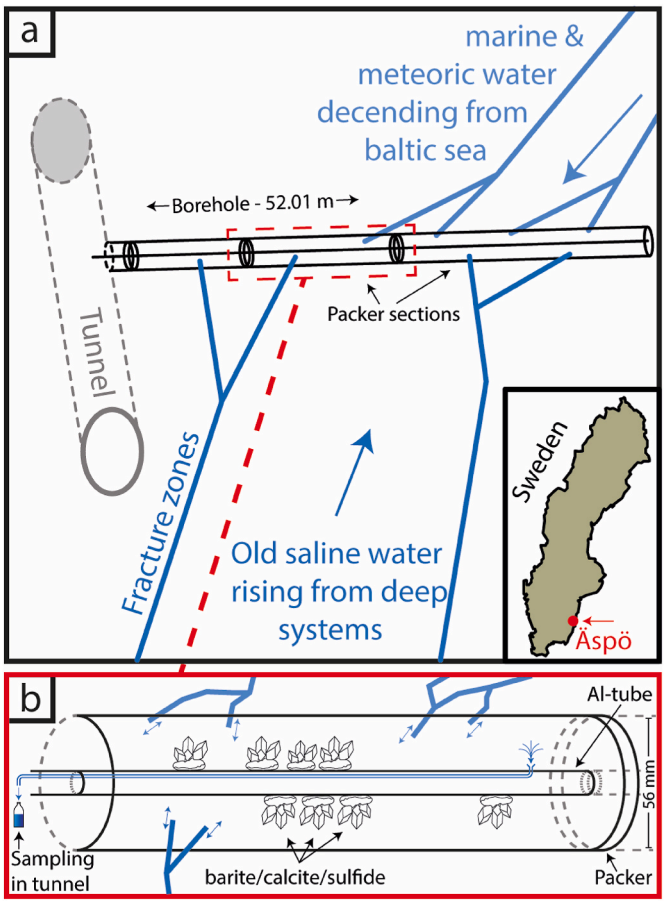

Fig. 1. a: Schematic figure of borehole drilled from Äspö tunnel and subdivision into packer sections. Water from different fractures supply the sections. Borehole A spans the length of 52.01 m, borehole B of 34.18 m. More detailed information is provided in Drake et al., (2018). b: Detailed packer section with Al-rod and precipitated minerals on borehole instrumentation.

groundwater within the fractures. It is acknowledged that stagnant water may have undergone potential manipulation by the borehole instrumentation over time. The temperature was consistently at 14 °C, and the pH values remained stable within the range of 7.4–7.7.

After 17 years, the borehole instrumentation was retrieved. Subsequently, calcite, sulfates, and Fe-sulfides were carefully scraped off the instrumentation (Fig. 1b) and collected in nitrogen-filled gas-tight bags to prevent oxidation. The samples analyzed in this study originate from both boreholes A and B. The names are coded as follows: boreholes A and B are denoted by A and B, respectively. Since the boreholes contain different sections supplied by various fracture waters, the section number occupies the second position. The third position indicates the sample number within that section. For example, sample A-3-1 originates from borehole A, section 3, crystal number 1. The section numbers relate to the detailed descriptions in Drake et al. (2018).

The fluid chemistry data was retrieved from SKB's quality-controlled database Sicada and described in Drake et al. (2015, 2018) and Yu et al. (2019). A set of relevant data is provided in ESM Data-3.

2.2. Analytical techniques

2.2.1. Scanning electron microscope

The scraped-off precipitates were loosely placed on Cu tape and investigated using a Hitachi S–3400 N scanning electron microscope (SEM) equipped with an Oxford INCA energy dispersive spectrometry (EDS) detector in low-vacuum mode, at University of Gothenburg, Sweden. After this inspection, barite could be localized and then handpicked with tweezers under the stereomicroscope. The handpicked crystals were mounted in epoxy, which was polished until the crystal interiors were exposed. The barite was then investigated again with the SEM to identify any zonation, cracks, or impurities prior to SIMS analysis.

2.2.2. Secondary ion mass spectrometry

Stable S and O isotopes in barite can be used to understand origin and temporal variation of the sulfate source and were determined within single crystals using a Cameca IMS1280 SIMS, at the NordSIMS facility at Museum of Natural History, Stockholm, Sweden. Separate analytical routines applied for S and O, are described briefly below, and closely follow those described by Whitehouse (2013) for sulfur, with the exception that only $^{34}S/^{32}S$ ratios were measured here, and Heinonen et al. (2015) for oxygen. For both elements, the samples were sputtered using a Gaussian focussed $^{133}Cs^{+}$ primary beam with 20 kV incident energy (10 kV primary, −10 kV secondary) and primary beam current of ~3 nA, which was rastered over a 5 × 5 μm area during analysis to homogenize the beam density. The resulting analytical crater had a diameter of ~10 μm. A normal incidence electron gun was used for charge compensation. Analyses were performed in automated sequences, with each analysis comprising a 40 s pre-sputter to remove the gold coating over a rastered 15 × 15 μm area, centering of the secondary beam in the field aperture to correct for small variations in surface relief, and data acquisition in twelve 4-s integration cycles. The magnetic field was locked at the beginning of the session using an NMR field sensor. Secondary ion signals (^{32}S and ^{34}S or ^{16}O and ^{18}O) were detected simultaneously using two Faraday detectors with a common mass resolution of 4860 (M/ΔM) for S and 2430 (M/ΔM) for O. The Fig Tree Bay reference material (Reuschel et al., 2012), with a conventionally determined $\delta^{34}S_{CDT}$ value of 4.5‰ and $\delta^{18}O_{CDT}$ value of 6.77‰ was used as a matrix-matched reference. Typical precision on a single $\delta^{34}S$ and $\delta^{18}O$ values, after propagating the within run and external uncertainties from the standard measurements was ±0.2‰ (1σ). All results are reported with respect to the V-CDT (Ding et al., 2001) and V-SMOW (Coplen, 1994) for oxygen.

2.2.3. Micro X-ray fluorescence

Major and trace element mapping was performed on polished barite samples with a Bruker M4 Tornado μ-XRF at the MAGMA Lab of the TU Berlin. The instrument is equipped with an X-ray capillary optic system and two 30 mm^2 silicon drift detectors. A spot size of 20 μm was used, the Rh-anode was operated at 50 kV acceleration voltage and the anode current of 600 mA at a chamber vacuum of 20 mbar was used. Spots were applied in 20 μm intervals and measured for 40 ms, resulting in a total mapping time of approx. 18 h for the entire mount. The energy position of the fluorescence lines and the power of the X-ray tube are calibrated monthly, using a set of single element standards provided by Bruker (Germany). This procedure enabled the semi-quantitative determination of trace element distribution and the identification of areas for the quantitative determination using LA-ICP-MS.

2.2.4. Laser ablation ICP-MS mappings

High-resolution LA-ICP-MS mapping was performed at the MAGMA Lab of the TU Berlin using an Agilent 8900 ICP-MS/MS coupled to an Analyte Excite 193 nm excimer laser (Teledyne Photon Machines). Helium is used as a carrier gas with a total flow rate of 0.95 l/min (0.5 l/min cell flow, 0.45 l/min cup flow).

After plasma ignition and initialization of Helium flow, m/z = 42 (e.g., $^{14}N^{14}N^{14}N^{+}$) and m/z = 31 (e.g., $^{15}N^{16}O$) were recorded to monitor the amount of air entrained in the interface tubing and ablation cell. After counts were stable and below 20 000 cps, the Ar nebulizer gas and He carrier gas flows were tuned to achieve m/z = 248/232 ratios of <0.05 % (ThO/Th) and m/z = 232/238 ratios of 100 ± 1 % (Th/U) while ablating NIST 610 in line scan mode. Small amounts (3–4 ml/min) of high-purity (99.999 %) N_2 were admixed to the Ar nebulizer gas to

increase sensitivity. Once stable plasma conditions were reached, an automatic lens tune was performed on NIST 610 to maximize sensitivity in the mid-mass range.

The aerosol rapid introduction system ARIS (Teledyne Photon Machines) was used. In cases where more than 4 elements were mapped, a low-volume adapter from Glass Expansion is added to the interface to increase the single pulse response (SPR), i.e. the combined wash-in and wash-out. The SPR was monitored by ablating NIST 610 glass at 1 Hz and dosage 1 in line scan mode and recording m/z = 238 (U) with a dwell time of 5 ms. By averaging the peak shape of 300 single pulses, the SPR was determined at the full width at 10 % of the maximum intensity and was between 30 ms (without adapter) and 120 ms (with adapter).

For mapping the elemental distribution within the target grain, at least four mass channels m/z = 88 (Sr), m/z = 137 (Ba), m/z = 139 (La), m/z = 238 (U) were recorded. For some mappings additionally m/z = 23 (Na), m/z = 89 (Y), m/z = 143 (Nd) and m/z = 172 (Yb) were measured.

Altogether fifteen grains were mapped using a raster of unidirectional scans with no overlap between lines and a 2 s pause after each line to prevent memory effects. Fluence was 1.5 J/cm^2, spot sizes were between 2 and 3 μm, the applied dosage was 10 (meaning a 10-fold spot overlap), repetition rates were between 83 and 167 Hz, and scan speeds between 24.9 μm/s and 33.4 μm/s. These parameters were chosen to suppress aliasing effects. Dwell times were distributed to achieve a signal/noise ratio larger than 20 for each mass channel based on test line scans on target grains. The total sweep time was tuned to avoid carry over of aerosol beyond the laser spot diameter during scanning. The ablation depth is limited to approx. 1–2 μm for the dosage applied, which allows repeated mappings of the same area.

All the raw data processing was performed using the software HDIP (Teledyne Photon machines). Background was corrected using a cubic spline function. To obtain quantitative mappings, each pixel is calibrated using multiple (at least 10) line scans on the reference material NIST 612, recorded before and after mapping of the target grain. In a second step, 2D segments within barite were defined to derive normalization factors so that the mean Ba content of the segment matches the one of stoichiometric $BaSO_4$ (Ba = 58.84 wt%). This normalization factor was also applied to all other pixels outside the segment. Drift was monitored and corrected using NIST612 line scans, but usually was negligible.

Minor differences in the crystal shape observed between SEM images and LA-ICP-MS mappings is attributed to an intermediate polishing step to remove the carbon coating (e.g., sample A-3-1; Fig. 2a and 3d).

2.2.5. Laser ablation ICP-MS spot analysis

Due to the small laser spot sizes applied for the trace element mappings, the detection limit is limited as well as the number of elements that can be recorded simultaneously, due to the sequential measurement mode of the ICP ś quadrupoles. To extent the available compositional information, additional LA-ICP-MS spot analyses with larger spot size have been applied on grains after the LA-ICP-MS mappings.

For spot analysis, a reduced repetition rate of 10 Hz and a large volume adapter from Glass Expansion was applied. Mass channels analyzed during spot analysis are m/z = 7 (Li), m/z = 23 (Na), m/z = 24 (Mg), m/z = 27 (Al), m/z = 28 (Si), m/z = 29 (K), m/z = 44 (Ca), m/z = 55 (Mn), m/z = 56 (Fe), m/z = 60 (Ni), m/z = 64 (Zn), m/z = 85 (Rb), m/z = 88 (Sr), (Y), m/z = 95 (Mo), m/z = 133 (Cs), m/z = 137 (Ba), m/z = 139 (La), m/z = 140 (Ce), m/z = 141 (Pr), m/z = 146 (Nd), m/z = 147 (Sm), m/z = 151 (Eu), m/z = 157 (Gd), m/z = 159 (Tb), m/z = 163 (Dy), m/z = 165 (Ho), m/z = 166 (Er), m/z = 169 (Tm), m/z = 172 (Yb), m/z = 175 (Lu), m/z = 238 (U). A single spot analyses consisted of 30 s gas blank, 40 s of ablation and a 30 s wash out period. The total sweep time is 0.3426 s. All elements are calibrated using NIST612 and Ba as an internal standard. Raw data were processed with HDIP.

2.2.6. Partition coefficient calculation

The calculation of partition coefficients is based on the formula

$$P_{Me} = (Me/Ba)_{barite}/(Me/Ba)_{solution} \quad (1)$$

with Me being the molar concentration of the element of interest normalized to the molar concentration of barium.

For the calculation of P_{Me} from LA-ICP-MS mappings, only the youngest barite growth zonation (YZ) was taken into account, since this zone is assumed to be equilibrated with the sampled fluid. This YZ is defined by the enriched Sr content compared to the core structures. Fluid concentration data of the appropriate fracture fluids was used for calculations. The average composition of this zone is obtained by calculating the mean value of all pixels within a certain sub-segment, termed region of interest (ROI) (see Fig. 3a and b, dashed green area). The measurement uncertainty is defined as the standard error of all pixel values (standard deviation divided by the square root of the number of pixel) and is typically between 0.5 and 2.5 %. For the spot analysis derived P_{Me}, element concentration data from the spot analysis was considered, respectively.

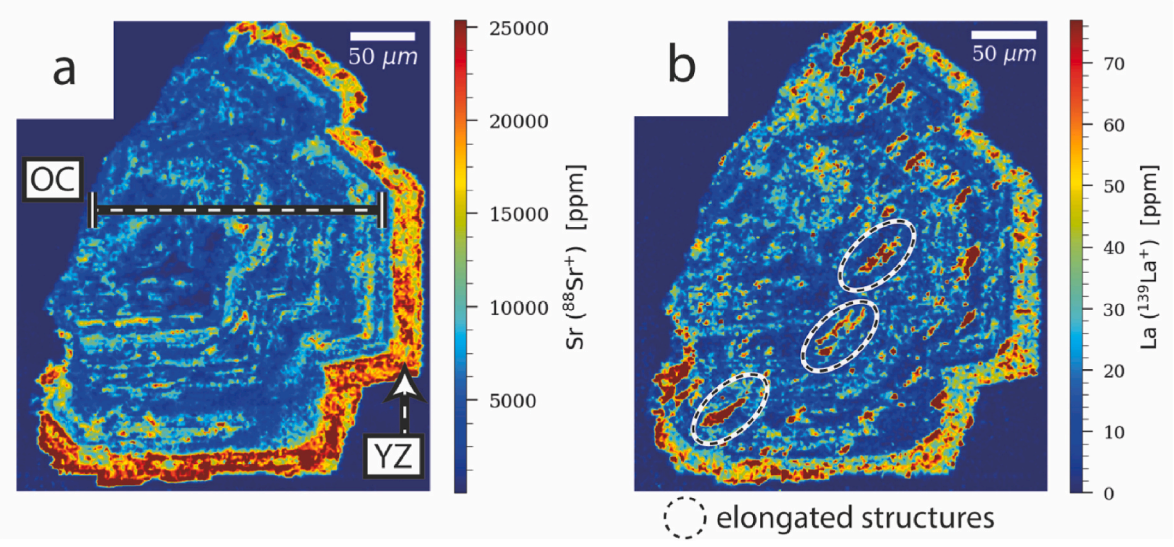

Fig. 2. Element distribution mappings of sample A-3-1 for the elements Sr and La. Fig. a indicates the oscillatory core (OC) and youngest zonation (YZ). Elongated structures are marked in fig. b.

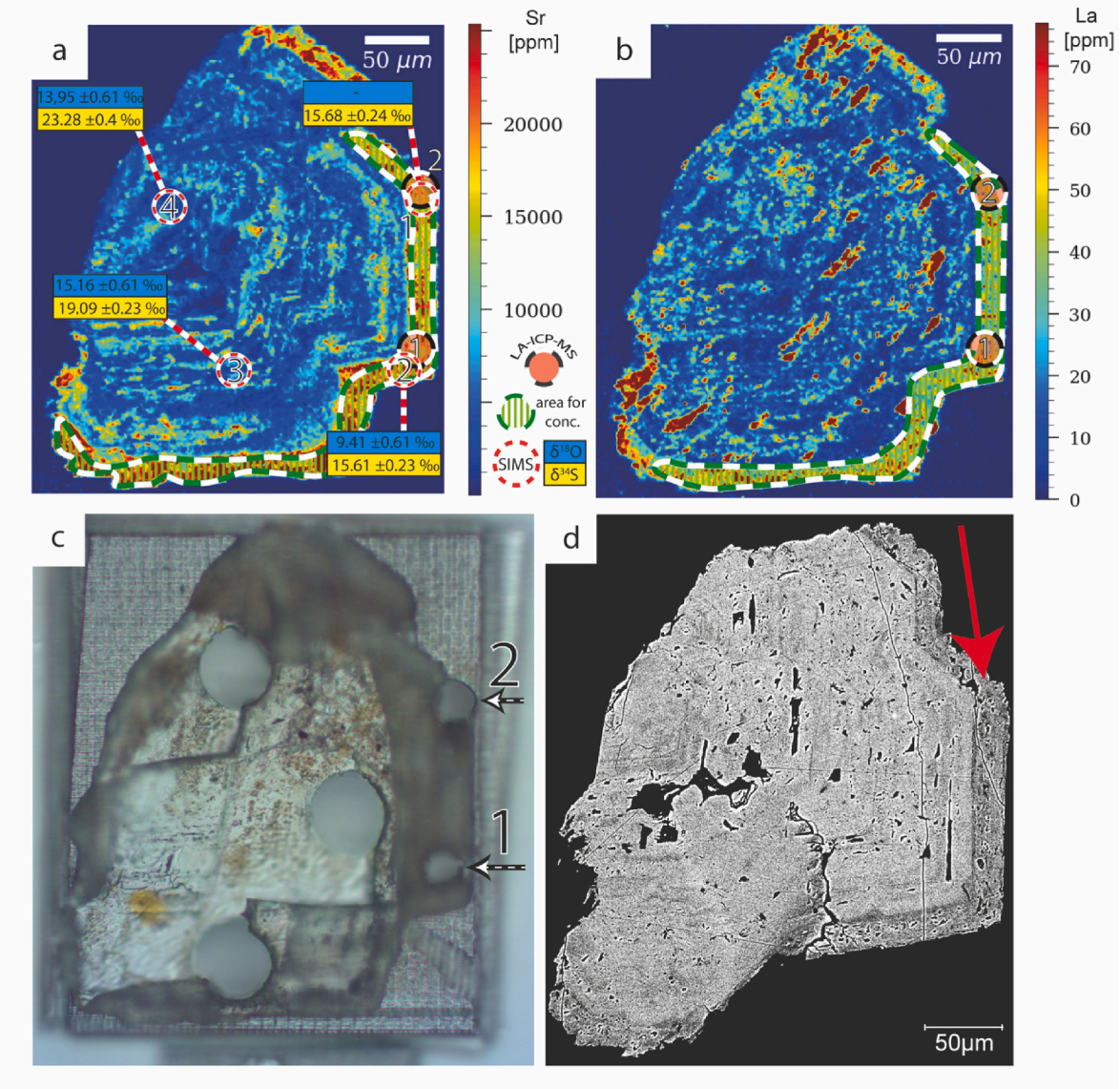

Fig. 3. a) Sr distribution map of sample A-3-1 with LA-ICP-MS spot analyses and SIMS spots. The dashed green area was used for integrated pixel average calculation for Sr concentration. b) La distribution map with LA-ICP-MS spots and concentration calculation area. c) Microscope image of sample A-3-1 after mapping and spot analysis. The remnants of multiple mappings are visible, and the laser pits used for this study are marked. d) SEM BSE image of sample A-3-1 with red arrow marking the darker areas with enhanced porosity.

2.2.7. *DFT simulation*

To evaluate the uptake behavior of Ra into barite based on the data collected for Sr, DFT simulations were performed. The computed difference between the partition coefficients of Ra and Sr allows to determine P_{Ra} based on P_{Sr} measured for the natural samples.

The DFT calculations were performed with the plane-wave Quantum-ESPRESSO code (Gianozzi et al., 2009), using the PBE exchange-correlation functional (Perdew et al., 1996). We applied the plane-wave energy cutoff of 50 Ryd and ultrasoft pseudopotentials to mimic the presence of core electrons (Vanderbilt, 1990). $BaSO_4$ phases have been computed with 2 × 2 × 2 supercells containing 192 atoms. The 2 × 2 × 2 Monkhorst-Pack *k*-points mesh was applied to assure converged results (Monkhorst and Pack, 1976). All structures were optimized with convergence thresholds of 10^{-5} Ry and 10^{-4} Ry/a_0 (where a_0 is the Bohr radius) for energy and forces, respectively. For the calculation of the cation exchange energy, we computed the structures doped with single impurity cation (Ra, Sr).

For the computation of the partition coefficient, the free energy (ΔG) of the following exchange reaction between a single cation M in the aqueous phase and one Ba^{2+} ion in one mol of barite was computed:

(2) $\boldsymbol{M^{2+}_{aq} + BaSO_4 \rightarrow M{:}BaSO_4 + Ba^{2+}_{aq}}$,

and the partition coefficient (P) is given by:

(3) $\boldsymbol{P = \exp(-\Delta G/K_bT)}$,

with kb being the Boltzmann constant and T being the temperature.

To estimate the ΔG, the values of the enthalpy of reaction 2 were estimated with the combination of DFT energies of the barite solid phases and M^{2+} and Ba^{2+} cations in the vacuum, and measured hydration energies of Ba^{2+} and M^{2+} = Ra^{2+}, Sr^{2+} cations. The hydration energies of the cations reported in literature are −1443 for Sr, −1305 for Ba and −1266 for Ra (Smith, 1977). We note that, while for Ba^{2+} and Sr^{2+} the measured values can be taken as accurate, the reported hydration energies of Ra^{2+} are more uncertain (Smith, 1977; Marcus, 1991). In this work we calibrated this value, so it reproduces the partitioning of Sr^{2+} and Ra^{2+} in C–S–H phases (Lange et al., 2018; Kowalski

et al., 2020). The resulting free energy of hydration of Ra^{2+} is −1255 kJ/mol, which is consistent with values provided by Marcus (1991).

In order to estimate the free energies of the cation exchange reactions, the entropy of the aqueous species of Shock et al. (1997) was applied. The entropy difference between pure and *M*-doped $BaSO_4$ was estimated from the difference of elemental entropy of Ba^{2+} and M^{2+} species as estimated by Latimer (1951). The same procedure was applied in our previous studies on Ra and Sr cation exchange in C–S–H phase (Lange et al., 2018; Kowalski et al., 2020).

3. Results

3.1. Morphology and internal structure of barite crystals

Barite occurs as both intact and fragmented euhedral crystals with oscillatory growth structures as displayed by SEM (Fig. 3d; electronic supplementary material (ESM) SEM images of A-2-1, A-2-5, A-3-3, B-1-1, B-1-4). Mineral size varies between 50 and 400 μm and some crystals exhibit a porous structure with pores having a diameter of up to 20 μm. The different brightness of growth zones, from SEM backscatter electron (BSE) images, indicates their variable chemical composition (Fig. 3d). The majority of the grains (12 of 13 grains; all presented crystals in ESM except B-1-2) show a distinct dark youngest zonation (YZ) in the BSE images with a thickness up to 20 μm, which grows on top of an oscillatory zoned core (OC), marked by alternating BSE-dark and BSE-light bands (Fig. 3d, red arrow). All grains have visible macroscopic pores all over the crystal. Larger pores, with an irregular distribution, attain diameters of up to 20 μm, while smaller elongated pores are discernible, aligning with the growth pattern (e.g., ESM crystal A-3-3). Noteworthy is the observation that the BSE-dark zones predominantly exhibit a greater density of pores compared to the BSE-light zones (e.g., ESM crystals A-2-2, A-2-3, A-2-5, A-3-2).

3.2. Distribution of Sr and La in natural barite and P_{Me} values

The LA-ICP-MS element mappings (Fig. 2a and b; ESM) show significant differences in the distribution of Sr and La within the barite crystals. Most crystals exhibit oscillatory zoning of Sr in the OC, which is barely displayed by La. There is no discernible positive or negative correlation between the incorporation of Sr and La. The highest Sr values, exceeding 30.000 ppm, are observed in the YZ, whereas the OC displays variations ranging from 1.500 ppm to 15.000 ppm. La is typically much less concentrated in barite ranging from 2 to 20 ppm in the OC, with contrasting values in the YZ, which is sometimes enriched (15–100 ppm; e.g., Fig. 2b; ESM crystals A-2-2, A-2-4) compared to the OC and sometimes not (5–20 ppm; e.g., ESM crystals A-3-2, B-1-1, B-1-2). Elemental distribution maps reveal La enrichments that form linear elongated features with concentrations exceeding 80 ppm (highest ca. 580 ppm), and a preferred orientation (e.g., Fig. 2b diagonally from top right to lower left; ESM crystals A-3-3, B-1-1, B-1-2). Notably, most instances of these linear features show positive correlation with Sr incorporation, attaining concentration levels comparable to those of the YZ (ESM crystals A-2-1, A-2-3, A-3-2, A-3-3). These structures crosscut the growth zonation in OC and YZ. Individual features extend up to 50 μm in length and 5 μm in width; however, no discernible traces of these structures are apparent in the SEM images, except when these structures are accompanied with elevates Sr concentrations (e.g., ESM crystal A-2-3).

The calculated P_{Sr} values for element mappings are presented in Table 1 and vary between 8.67×10^{-5} and 3.21×10^{-4} with a mean value of 1.66×10^{-4}. P_{La} values vary between 5.80×10^{-3} and 6.72×10^{-2} with a mean value of 4.28×10^{-2}.

3.3. LA-ICP-MS spots

The small laser beam sizes and low dosages applied essentially limit the number of elements that can be acquired with reasonable sensitivity and precision during a particular mapping session. Hence, we conducted a re-analysis of the mapped grains, which involved employing conventional static spot ablation with larger beam diameters ranging from 25 to 50 μm. This way, the conventional method of LA-ICP-MS spot analysis was applied to test the accuracy of the mapping method. The placement of the spots was guided by the readily obtained element distribution maps. Only the time-resolved signal of two 25 μm spot analyses (A-3-1 spot 1 and 2) from barite sample A-3-1 (Fig. 3a) displayed a monotonic decrease in trace element count rate. For these analyses we are confident that the signal is derived only from the YZ and does not penetrate the OC at depth. This is supported by the agreement of the Sr concentration and hence P_{Sr} calculated for spot and mapping analyses (Fig. 4) with an average value of $1.96 \times 10^{-4} \pm 4.87 \times 10^{-5}$ over spots 1 and 2. The La concentrations between mapping and spot analysis in A-3-1 spot 2 are in agreement; however, spot analysis A-3-1 spot 1 resulted in slightly higher La concentrations and P_{La}, respectively ($1.05 \times 10^{-2} \pm 5.60 \times 10^{-3}$; ESM Data-1). Additional elements were analyzed and concentration data is provided in ESM-Data 2.

Table 1
Calculated partition coefficients for Sr and La based on integrated pixel average in defined element mapping areas (Fig. 3a and b; ESM).

sample	P_{Sr}	P_{La}
A-2-1	$1.63 \times 10^{-4} \pm 2.8 \times 10^{-5}$	$4.09 \times 10^{-2} \pm 1.0 \times 10^{-2}$
A-2-2	$2.05 \times 10^{-4} \pm 3.5 \times 10^{-5}$	$6.65 \times 10^{-2} \pm 1.9 \times 10^{-2}$
A-2-3	$9.61 \times 10^{-5} \pm 1.7 \times 10^{-5}$	$1.66 \times 10^{-2} \pm 4.1 \times 10^{-3}$
A-2-4	$2.42 \times 10^{-4} \pm 4.2 \times 10^{-5}$	$5.35 \times 10^{-2} \pm 1.7 \times 10^{-2}$
A-2-5	$1.16 \times 10^{-4} \pm 2.0 \times 10^{-5}$	$4.81 \times 10^{-2} \pm 1.2 \times 10^{-2}$
A-2-6	$1.70 \times 10^{-4} \pm 2.9 \times 10^{-5}$	$6.72 \times 10^{-2} \pm 1.6 \times 10^{-2}$
A-3-1	$1.71 \times 10^{-4} \pm 2.9 \times 10^{-5}$	$7.17 \times 10^{-3} \pm 1.7 \times 10^{-3}$
A-3-2	$2.30 \times 10^{-4} \pm 5.3 \times 10^{-5}$	$5.80 \times 10^{-3} \pm 1.4 \times 10^{-3}$
A-3-3	$3.21 \times 10^{-4} \pm 5.5 \times 10^{-5}$	$1.63 \times 10^{-2} \pm 4.1 \times 10^{-3}$
B-1-1	$8.67 \times 10^{-5} \pm 1.5 \times 10^{-5}$	$6.06 \times 10^{-2} \pm 1.5 \times 10^{-2}$
B-1-2	$1.05 \times 10^{-4} \pm 1.8 \times 10^{-5}$	$6.16 \times 10^{-2} \pm 1.8 \times 10^{-2}$
B-1-3	$1.54 \times 10^{-4} \pm 2.7 \times 10^{-5}$	$6.37 \times 10^{-2} \pm 1.6 \times 10^{-2}$
B-1-4	$9.89 \times 10^{-5} \pm 1.7 \times 10^{-5}$	$4.86 \times 10^{-2} \pm 1.2 \times 10^{-2}$
Mean P_{Me}	1.66×10^{-4}	4.28×10^{-2}
RSD (%)	33.3	50.9

3.4. Sulfur and oxygen isotope signatures in natural barite

Stable sulfur and oxygen isotope ratios vary within the barite crystals. The $\delta^{34}S$ values for sample A-3-1 (Fig. 3a) decrease from 23.28‰ to 19.09‰ in the OC, to 15.61‰ in YZ. The respective $\delta^{18}O$ values show a similar trend with values from 13.95‰ to 15.16‰ in the OC and decreasing to 9.41‰ in the YZ. These variations may be explained by different water sources or their mixing ratios that were in contact with the barite crystals during precipitation. In this respect, it cannot be assumed that the hydrochemical conditions were constant during the 17-year formation phase of the barite crystals.

3.5. Natural Ra partition coefficients from DFT calculations

The computed free energy of reaction 2 and the relevant thermodynamic parameters are provided in Table 2. Here we assumed that the enthalpy of cation exchange reaction is independent of the temperature. This approach is justified as the difference in the dissolution enthalpy between Ba and Sr or Ra shows very week temperature dependence (Vinograd et al., 2018a). A large difference for the partition between Ba–Sr and Ba-Ra pairs is expected because of large entropy difference between the two species in the aqueous phase of 85.4 J/mol/K (Shock et al., 1997), which transfers to about 26 kJ/mol difference in free energy at ambient conditions. The results suggest that the partition coefficient for the Ba-Ra pair is by about two orders of magnitude larger than that for the Ba–Sr pair. Based on the determined P_{Sr} data, a P_{Ra} value in the 10^{-2} range for barite in the Äspö complex is obtained (Table 2).

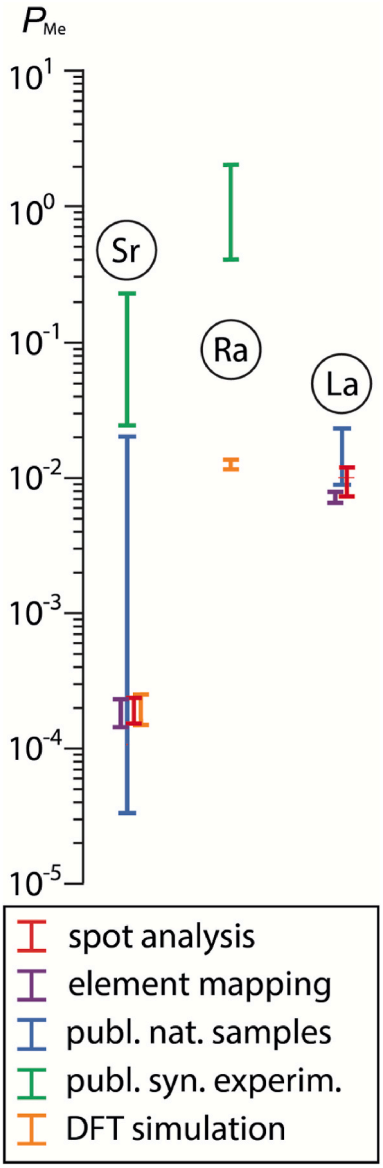

Fig. 4. Derived partition coefficient values of sample A-3-1 spot 2 (red), mapping results for the youngest overgrowth zonation of sample A-3-1 (purple) and DFT simulated P_{Sr} and P_{Ra} (orange) for a temperature range of 14–27 °C. For comparison, existing values for natural barite samples and synthetic experiments of similar ambient temperatures are included into the figure in blue and green (Doerner and Hoskins, 1925; Gordon and Rowley, 1957; Averyt and Paytan, 2003; Curti et al., 2010; Rosenberg et al., 2014; Widanagamage et al., 2014; Brandt et al., 2015; Jamieson et al., 2016; Heberling et al., 2018).

The temperature dependence of P_{Ra} is significantly weaker compared to P_{Sr}. This is due to the fact that the reaction enthalpy for Ra exchange is quite small, which makes the partition coefficient derived by equation (3) nearly constant. This is the expected result, as Ra is very similar in size to Ba and both species have very similar hydration. However, the final results are highly sensitive to the uncertainties of the computed and measured data. 5 kJ/mol uncertainty in free energy (ΔG) would produce a difference of one order of magnitude in the predicted partition coefficients. DFT-predictions with lower uncertainties can be calculated by having accurate measurements of the hydration enthalpy and free energy of Ra^{2+}.

Table 2
The computed enthalpy, entropy and free energy of cation exchange reaction 2 at different temperatures. The resulting partitioning coefficients are reported in the last column. ΔH is DFT reaction enthalpy, -TΔS is entropy, ΔG is Gibb's free energy.

temperature	cation	ΔH [kJ/mol]	-TΔS [kJ/mol]	ΔG [kJ/mol]	P_{Me}
275K/2 °C	Sr	30.8	−9.3	21.4	8.5 x10^{-5}
	Ra	0.4	+9.8	10.2	1.1 x10^{-2}
287K/14 °C	Sr	30.8	−9.8	21.0	1.5 x10^{-4}
	Ra	0.4	+10.2	10.6	1.2 x10^{-2}
300K/27 °C	Sr	30.8	−10.2	20.6	2.6 x10^{-4}
	Ra	0.4	+10.7	11.1	1.2 x10^{-2}
525K/252 °C	Sr	30.8	−17.9	12.9	4.3 x10^{-3}
	Ra	0.4	18.6	19.0	1.3 x10^{-2}

4. Discussion

4.1. Partitioning of Sr and Ra between barite and aqueous fluid

Unlike laboratory experiments that often emulate closed systems, natural fluid systems undergo substantial changes in physicochemistry, primarily due to fluid mixing. In the Äspö HRL region, Mathurin et al. (2012) described the presence of at least four identifiable fluid end-members, revealing a complex history of transport and mixing. Sulfur and oxygen isotope composition of the barite in microscale gives further input to the understanding of fluid evolution and mixing in the boreholes. While temperature and pH remained stable at the Äspö boreholes (Drake et al., 2018), oxygen and sulfur isotope values decrease significantly from older growth zones ($\delta^{34}S$ = 23.28‰, $\delta^{18}O$ = 13.95‰) to younger growth zones ($\delta^{34}S$ = 15.61‰; $\delta^{18}O$ = 9.41‰). The higher isotope values in the older grain parts likely reflect a stronger contribution of fracture water and/or Modern Baltic Seawater, which has a $\delta^{34}S$ of 21‰ (Böttcher and Huckriede, 1997). Fracture and stagnant Äspö water samples collected in 2012 exhibit even higher $\delta^{34}S$ values of 28.6‰ and 26.5‰, respectively (Drake et al., 2015). This sulfur isotope enrichment confirms ongoing bacterial sulfate reduction, as described in previous studies (Wallin, 2011; Drake et al., 2015). Conversely, the lower $\delta^{34}S$ value of 15.6‰ in the outermost rim indicates a stronger contribution from ascending old saline water, which is thought to have a $\delta^{34}S$ value of around 10‰ (Wallin, 2011). This observation aligns with the higher Sr concentrations found in the younger rim structures. The SIMS results indicate, that over the course of the 17-year experiment, the fluid mixture transitioned form being dominated by Baltic Seawater to experiencing a stronger influx of rising saline waters.

Consequently, the OC and YZ represent two distinct growth events within the packer sections: In the initial stages of the experiment, the OC formed with fewer pores and oscillatory zoned structures. The connection between the observed oscillatory patterns and previously documented barite zoning (Putnis et al., 1992; Prieto et al., 1993) or their association with frequent discharges of the packer sections remains unclear. At a later point of the experiment, a change in fluid composition led to relatively faster precipitation, resulting in the formation of the YZ with additional pores and increased Sr uptake (e.g., Fig. 2a and 3d; ESM crystals A-2-4, B-1-1, B-1-3, B-1-4).

By using the average Sr concentration within the YZ and the concentration data of the fluid in contact with the barite, P_{Sr} values in the upper x10^{-5} to x10^{-4} range were calculated (Table 1, Fig. 4). Previous

studies have determined P_{Sr} values for natural barite in a marine setting (P_{Sr} 2.9 x10^{-5} ±6.4 x10^{-6}, T = 4°C, Averyt and Paytan, 2003) and for hydrothermal conditions (P_{Sr} 1 x10^{-3} - 1 x10^{-2}; T = 61–301°C; Jamieson et al., 2016), suggesting a positive correlation between temperature and P_{Sr}. This trend, previously outlined by Hanor (2000), is supported by the P_{Sr} determined by this study (T = 14 °C), which fall somewhere in between the published values (Fig. 5). A similar T - P_{Sr} trend is displayed by the data obtained for synthetic barite (Fig. 5; T = 5–40 °C, P_{Sr} = 0.01–0.17; Widanagamage et al., 2014). Notably, the P_{Sr} values for synthetic barite are offset by ~2-3 orders of magnitude towards higher values compared to the P_{Sr} of natural barite (Fig. 5).

DFT simulations predict a P_{Sr} value consistent with the P_{Sr} value calculated using the LA-ICP-MS mapping method. The corresponding DFT-derived P_{Ra} value falls within the 10^{-2} range, as shown in Table 2. Previously published laboratory based P_{Ra} values for barite fall within the range of 0.12–2.1, indicating a significantly higher Ra uptake capability (Fig. 4; Doerner and Hoskins, 1925; Gordon and Rowley, 1957; Curti et al., 2010; Rosenberg et al., 2014; Brandt et al., 2015; Heberling et al., 2018). This discrepancy of ~1-2 orders of magnitude between the partition coefficients measured in situ for synthesized barite and for natural samples can be attributed to two scenarios:

First, laboratory-derived P_{Ra} values originate from supersaturated solutions (with respect to $RaSO_4$) developing towards conditions close to equilibrium (CTE) during the experiments, as evidenced in studies like those conducted by Doerner and Hoskins (1925), Brandt et al. (2015) and Heberling et al. (2018). The Äspö fluid in contact to the barite samples, however, was characterized by Fichtner et al. (2024) to conditions CTE with respect to barite (saturation index = −0.093 to 0.107). It is conceivable that higher initial saturation states of laboratory experiments contribute to increased growth rates, as proposed by Vital et al. (2020). Notably, Weber et al. (2018) observed a decline in Sr uptake at slower growth rates, potentially explaining the observed disparity in Sr partitioning between faster precipitating synthetic and slower precipitating natural systems. Considering that the DFT-based estimates of P_{Ra} depend on the computed P_{Sr}, which is consistent with the values measured for natural samples, the obtained lower P_{Sr} implies lower P_{Ra}. It is important to note that Brandt et al. (2015) observed an opposite trend: a lower partitioning coefficient for elements compatible with the barite structure, during precipitation at elevated growth rates from highly supersaturated solutions.

Furthermore, the temperature has been identified as a parameter correlating positively with P_{Ra} (Rosenberg et al., 2011; Rosenberg et al., 2014), P_{Sr} (Fig. 5) and growth rates (Vital et al., 2020). Most experimental studies were conducted at ambient temperatures, differing from the 14 °C of the Äspö borehole system. This temperature difference could also account for the discrepancy and a higher temperature in Äspö would have resulted in higher P_{Sr} values and, consequently, elevated P_{Ra} values, albeit to a lesser extent.

Second, a discrepancy based on the uncertainty in the computed and measured thermodynamic data of this study cannot be excluded. The change of ~5 kJ/mol in the cation exchange free energy would reconcile this prediction with the above-mentioned data.

4.2. La as an indicator for trivalent actinide uptake in barite

Published P_{La} values for continental barite, ranging from 10^{-2} to 10^{-1} (Guichard et al., 1979) are in line with the P_{La} results of this study (Table 1). Moreover, the LA-ICP-MS element distribution mappings reveal elongated La and Sr enriched structures, crosscutting the internal growth structure of the barite crystal in multiple samples (Fig. 2b; ESM crystals A-2-4, B-1-1, B-1-2). For La, these accumulations reach the highest concentrations (>500 ppm) observed within the barite grains. This observation suggests a post-crystallization secondary process, with the preferably parallel alignment of these features indicating potential crystallographic control over their orientation. Similar elongated structures in synthetic barite, as documented by Weber et al. (2016), manifest as macropores following layered growth zonations. Weber et al. (2016) differentiated between macropores, which exhibit random orientation or align with crystal zonation, and nano-scale pores, primarily oriented parallel to the outer surface of the barite particles. Furthermore, Focused Ion Beam (FIB) tomography conducted by Weber et al. (2017) unveiled that the macropore system connects to the mineral surface, facilitating fluid ingress into the inner crystal. The Äspö barites exhibit elongated macropores of primary crystal growth (e.g., ESM crystals B-1-1, B-1-4), as well as secondary, potentially interconnected, macropores crosscutting the crystals growth zonation.

However, these are evidently independent of the elongated La enrichment process. Due to the explicit orientation, the La features in this study are more closely associated with cleavage planes, as opposed to the macropores following surface structures observed by Weber et al. (2016). Cleavage planes, identified as hosting macroscopic fluid inclusions (Rajabzadeh, 2007), may have also served as locations for the formation of nano-scale pores during mineral growth, as observed by Weber et al. (2016). Weber et al. (2017) describe these nano-scale pores to be distributed within the complete barite particles, providing a direct pathway for aqueous fluid to enter by diffusion. The resulting large surface area along the cleavage planes provides a conducive environment for the uptake of La, driven by the low segregation energy favoring

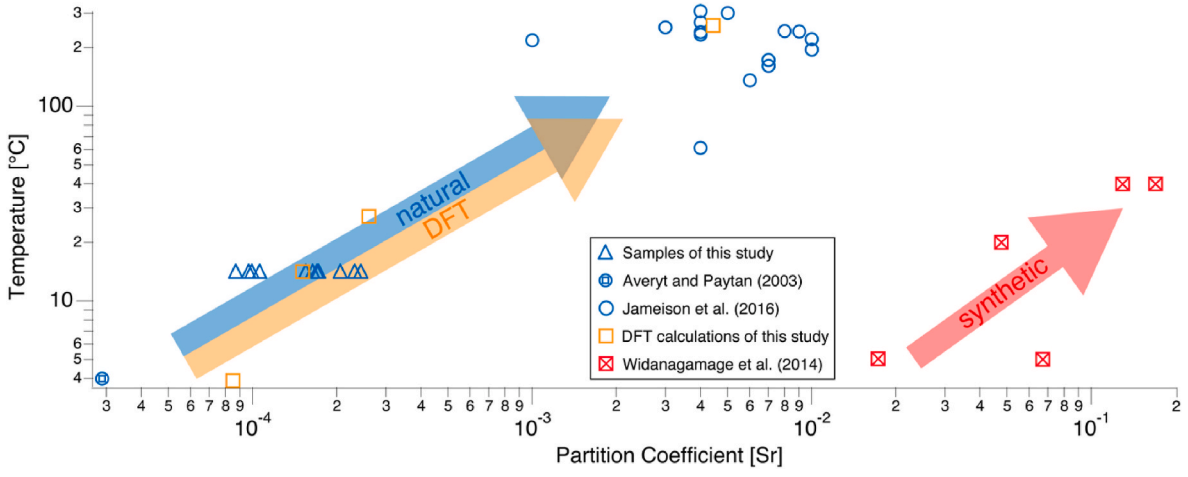

Fig. 5. Temperature dependency of P_{Sr} in natural (blue) and synthetic (red) barite, as well as DFT calculation values from this study (Table 2; yellow). The P_{Sr} values calculated in this study align with the temperature dependency of previous studies and show a discrepancy of approx. two orders of magnitude between natural and synthetic samples.

substitution on surface structures (Bunney et al., 2014). Bunney et al. (2014) observed incorporation through substitution of La into the barite surface structure with adjusted lattice parameters.

The convergence of the macroscopic pore system, enabling fluid entry into the barite, and its interconnection with the nano-scale pore system along cleavage planes could explain the origin of the elongated structures. The Sr concentrations in these structures reach levels similar to those observed in the YZ (e.g., ESM crystals A-2-3, A-3-2), suggesting the influx of the late-stage fluid responsible for YZ formation. Thus, La serves as a proxy for fluid paths into the nano-scale pore structures.

Due to analogous behavior, trivalent actinides are likely to follow a similar pattern of uptake into these elongated structures. Notably, the relative uptake of La within these structures surpasses that in the bulk crystalline structure by a factor ranging between 30 and 40 - a factor presumed to extend to trivalent actinides. The substantial uptake of La implies a significant retention capacity for actinides in the event of a failure in a waste repository.

5. Conclusions

This study has successfully addressed a critical knowledge gap providing environment-relevant partition coefficient data for various elements in a geological setting comparable to that of a nuclear waste repository. Two possible mechanisms for radionuclide retention were revealed via LA-ICP-MS element mappings:

First, incorporation of Sr into the zonation structures during barite formation, which can be linked to Ra incorporation due to the analogy of these elements. The concentration of Sr can vary significantly within the investigated barite minerals, most likely induced by fluid mixing. The presented DFT-derived P_{Ra} values state a high uptake capability of Ra in barite in the Äspö complex, but multiple factors, including the crystal growth rate and changing chemical fluid parameters over time can influence the Ra uptake in a real contaminated scenario.

P_{Ra} values from laboratory experiments indicate a higher uptake of Ra into barite compared to the estimated natural P_{Ra} values from this study. Consequently, partition behavior derived from laboratory experiments should be interpreted with caution, as they not necessarily reflect the nature. Furthermore, based on the DFT calculations, the positive temperature dependency observed for Sr uptake does not apply to Ra to the same extend. As a result, the temperature at a repository site with heat-emitting characteristics is according to the DFT results not a significant factor for Ra retention in barite.

The coexistence and concomitant effects of Ba, Sr and Ra on the partitioning behavior for barite in natural systems was neither investigated in the P_{Me}-based laboratory experiments, nor in the natural sample studies. Thermodynamic ternary studies ($(Ra,Sr,Ba)SO_4$) showed, that the presence of $RaSO_4$ in the system stabilizes the Ba-rich and destabilizes the Sr-rich SO_4-components (Vinograd et al., 2018a, 2018b). Brandt et al. (2020) confirmed these results with experimental studies and found, that already trace amounts of Sr in the solid solution can have a positive impact on the Ra uptake into barite. In a real-world scenario, where both Sr and Ra are present in solution, P_{Ra} might show variations in the presence of differing Sr concentrations in the system.

Second, La uptake shows a process of significant enrichment along elongated structures crosscutting the crystals growth zonation structure that can be transferred to potential trivalent actinide uptake. This secondary enrichment is most likely linked to the existence of nano-scale pore systems along cleavage planes, allowing fluid migration along these paths. High surface areas provided by connected nano-scale pore systems allow the settlement of La in these structures. The selective restriction of La to these structures, rather than accumulating in the YZ, may be attributed to the potential formation of a solid solution only within the initial layers of the surface. For La, this phenomenon appears to be exclusive to the interconnected pore system. Strontium was noted to exhibit access to the elongated structure system, demonstrating concentrations akin to those found in the most recent overgrowth. This observation suggests the migration of late-stage fluid migration into the barite, implying potential secondary alteration processes and concurrent fixation of not only trivalent actinides, but also Ra within the core crystal structure. The concentrations of Sr and especially La in these structures state a high potential for radionuclide retention, that requires further investigation in terms of quantity and occurrence.

The obtained results carry significant relevance for safety assessment modelling of repository sites, as they enhance the data's applicability and reliability within the models.

Declaration of generative AI and AI-assisted technologies in the writing process

During the preparation of this work the authors used ChatGPT in order to improve readability and language. After using this tool/service, the authors reviewed and edited the content as needed and take full responsibility for the content of the publication.

CRediT authorship contribution statement

Ferdinand Kirchner: Writing – original draft, Visualization, Validation, Software, Project administration, Methodology, Investigation, Formal analysis, Data curation, Conceptualization. **Martin Kutzschbach:** Writing – original draft, Supervision, Methodology, Investigation, Funding acquisition, Formal analysis, Data curation, Conceptualization. **Henrik Drake:** Writing – original draft, Validation, Resources, Methodology. **Vanessa Fichtner:** Writing – original draft, Validation, Resources, Methodology. **Piotr M. Kowalski:** Writing – original draft, Resources, Methodology, Investigation, Data curation. **Stefan Rudin:** Writing – original draft, Resources, Methodology, Investigation, Formal analysis, Data curation. **Martin J. Whitehouse:** Resources, Investigation. **Mikael Tillberg:** Methodology. **Thomas Neumann:** Writing – original draft, Validation, Supervision, Resources, Project administration, Methodology, Investigation, Funding acquisition, Formal analysis, Data curation, Conceptualization.

Declaration of competing interest

The authors declare the following financial interests/personal relationships which may be considered as potential competing interests: Thomas Neumann reports financial support was provided by Federal Ministry of Education and Research. Henrik Drake reports financial support was provided by Swedish Research Council. Henrik Drake reports financial support was provided by Swedish Research Council Formas. Henrik Drake reports financial support was provided by Crafoord Foundation. If there are other authors, they declare that they have no known competing financial interests or personal relationships that could have appeared to influence the work reported in this paper.

Acknowledgements

We thank Swedish Nuclear Fuel and Waste Management Company (SKB) for providing data of fluids (extracted from SKB database Sicada and from cited reports). This work was supported by the Federal Ministry of Education and Research (BMBF) joint research project KRIMI "Kinetik der Radionuklidimmobilisierung endlagerrelevanter Mischkristalle" (Grant No. 02NUK056D). HD was funded by the Swedish Research Council (#2021–04365), Formas – a Swedish Research Council for Sustainable Development (#2020-01577), and the Crafoord Foundation (#20210524). We thank Felix Brandt and Martina Klinkenberg (FZ Jülich, Germany) for fruitful discussions.

Appendix A. Supplementary data

Supplementary data to this article can be found online at https://doi.org/10.1016/j.apgeochem.2024.106208.

Data availability

Data will be made available on request.

References

van Acker, T., Van Malderen, S.J.M., Van Helden, T., Stremtan, C., Šala, M., van Elteren, J.T., Vanhaecke, F., 2021. Analytical figures of merit of a low-dispersion aerosol transport system for high-throughput LA-ICP-MS analysis. J. Anal. At. Spectrom. 36, 1201–1209. https://doi.org/10.1039/D1JA00110H.

Apted, M.J., Ahn, J., 2017. 1 – repository 101: multiple-barrier geological repository design and isolation strategies for safe disposal of radioactive materials. Woodhead Publ. series in energy 3–26. https://doi.org/10.1016/B978-0-08-100642-9.00001-3, 2017.

Averyt, K.B., Paytan, A., 2003. Empirical partition coefficients for Sr and Ca in marine barite: implications for reconstructing seawater Sr and Ca concentrations. Geochem. Geophys. Geosyst. 4, 1–14. https://doi.org/10.1029/2002GC000426.

Brandt, F., Curti, E., Klinkenberg, M., Rozov, K., Bosbach, D., 2015. Replacement of barite by a (Ba,Ra)SO_4 solid solution at close-ot-equilibrium conditions: a combined experimental and theoretical study. Geochim. Cosmochim. Acta 155, 1–15. https://doi.org/10.1016/j.gca.2015.01.016.

Brandt, F., Klinkenberg, M., Poonoosamy, J., Bosbach, D., 2020. Recrystallization and uptake of ^{226}Ra into Ba-rich (Ba,Sr)SO_4 solid solutions. Minerals 10, 812. https://doi.org/10.3390/min10090812.

Birkholzer, J., Houseworth, J., Tsang, C.F., 2012. Geologic disposal of high-level radioactive waste: status, key issues, and trends. Annu. Rev. Environ. Resour. 37, 79–106. https://doi.org/10.1146/annurev-environ-090611-143314.

Böttcher, M.E., Huckriede, H., 1997. First occurrence and stable isotope composition of authigenic γ-MnS in the central Gotland Deep (Baltic Sea). Mar. Geol. 137, 201–205. https://doi.org/10.1016/S0025-3227(96)00115-6.

Bunney, K., Freeman, S., Ogden, M.I., Richmond, W.R., Rohl, A.L., Jones, F., 2014. Effect of lanthanum on the crystal growth of barium sulfate. Cryst. Growth Des. 14, 1650–1658. https://doi.org/10.1021/cg401776e.

Coplen, T.B., 1994. Reporting of stable hydrogen, carbon, and oxygen isotopic abundances (Technical Report). Pure Appl. Chem. 66 (2), 273–276. https://doi.org/10.1351/pac199466020273.

Curti, E., 1999. Coprecipitation of radionuclides with calcite: estimation of partition coefficients based on a review of laboratory investigations and geochemical data. Appl. Geochem. 14, 433–445. https://doi.org/10.1016/S0883-2927(98)00065-1.

Curti, E., Fujiwara, K., Iijima, K., Tits, J., Cuesta, C., Kitamura, A., Glaus, M.A., Müller, W., 2010. Radium uptake during barite recrystallization at 23 +-2 °C as a function of solution composition: an experimental 122 Ba and 226 Ra tracer study. Geochim. Cosmochim. Acta 74 (12), 3553–3570. https://doi.org/10.1016/j.gca.2010.03.018.

Dares, C.J., Lapides, A.M., Mincher, B.J., Meyer, T.J., 2015. Electrochemical oxidation of ^{243}Am(III) in nitric acid by a terpyridyl-derivatized electrode. Science 350, 6261. https://doi.org/10.1126/science.aac9217 doi:10.1126/science.aac921.

Ding, T., Valkiers, S., Kipphardt, H., De Bièvre, P., Taylor, P.D.P., Gonfiantini, R., Krouse, R., 2001. Calibrated sulfur isotope abundance ratios of three IAEA sulfur isotope reference materials and V-CDT with a reassessment of the atomic weight of sulfur. Geochim. Cosmochim. Acta 65 (15), 2433–2437. https://doi.org/10.1016/S0016-7037(01)00611-1.

Doerner, H.A., Hoskins, W.M., 1925. Co-precipitation of radium and barium sulphates. J. Am. Chem. Soc. 47, 662–675. https://doi.org/10.1021/ja01680a010.

Drake, H., Tulborg, E.L., Whitehouse, M., Sandberg, B., Blomfeldt, T., Aström, M.E., 2015. Extreme fractionation and micro-scale variation of sulphur isotopes during bacterial sulphare reduction in deep groundwater systems. Geochim. Cosmochim. Acta 161, 1–18. https://doi.org/10.1016/j.gca.2015.04.014.

Drake, H., Mathurin, F.A., Zack, T., Schäfer, T., Roberts, N.M.W., Whitehouse, M., Karlsson, A., Broman, C., Aström, M.E., 2018. Incorporation of metals into calcite in a deep anoxic granite aquifer. Environ. Sci. Technol. 52, 493–502. https://doi.org/10.1021/acs.est.7b05258.

Durant, S.F., Ward, N.I., 2005. Recent biological and environmental applications of laser ablation inductively coupled plasma mass spectrometry (LA-ICP-MS). J. Anal. At. Spectrom. 20, 821–829. https://doi.org/10.1039/B502206A, 2005.

Fichtner, V., Kirchner, F., Kutzschbach, M., Strauss, H., Tillberg, M., Whitehouse, M., Drake, H., 2024. Microscale δ^{34}S and δ^{18}O variations of barite as an archive for fluid mixing and microbial sulphur metabolisms in igneous rock aquifers. Isot. Environ. Health Stud. https://doi.org/10.1080/10256016.2024.2410293.

Gianozzi, P., Baroni, S., Bonini, N., Calandra, M., Car, R., Cavazzoni, C., Ceresoli, D., Chiarotti, G., Cococcioni, M., Dabo, I., Corso, A., Gironcoli, S., Fabris, S., Fratesi, G., Gebauer, R., Gerstmann, U., Gougoussis, C., Kokalj, A., Lazzeri, M., Martin-Samos, L., Marzari, N., Mauri, F., Mazzarello, R., Paolini, S., Pasquarello, A., Paulatto, L., Sbraccia, C., Scandolo, S., Sclauzerp, G., Seitsonen, A., Smogunov, A., Umari, P., Wentzcovitch, R., 2009. QUANTOM espresso: a modular and open-source software project for quantum simulations of materials. J. Phys.: Condens. 21, 395502. https://doi.org/10.1088/0953-8984/21/39/395502.

Gordon, L., Rowley, K., 1957. Coprecipitation of radium with barium sulfate. Anal. Chem. 29, 1. https://doi.org/10.1021/ac60121a012.

Guichard, F., Church, T.M., Treuil, M., Jaffrezic, H., 1979. Rare earths in barites: distribution and effects on aqueous partitioning. Geochim. Cosmochim. Acta 43, 983–997. https://doi.org/10.1016/0016-7037(79)90088-7.

Hamlat, M.S., Kadi, H., Fellag, H., 2003. Precipitate containing norm in the oil industry: modelling and laboratory experiments. Appl. Radiation and Isotopes 59, 95–99. https://doi.org/10.1016/S0969-8043(03)00123-4, 2003.

Hanor, J.S., 2000. Barite-celestine geochemistry and environments of formation. Rev. Mineral. Geochem. 40 (1), 193–275. https://doi.org/10.2138/rmg.2000.40.4.

Heberling, F., Mets, V., Böttle, M., Curti, E., Geckeis, H., 2018. Barite recrystallization in the presence of ^{266}Ra and ^{133}Ba. Geochim. Cosmochim. Acta 232, 124–139. https://doi.org/10.1016/j.gca.2018.04.007.

Heinonen, A., Andersen, T., Rämö, O.T., Whitehouse, M., 2015. The source of Proterozoic anorthosite and rapakivi granite magmatism: evidence from combined in situ Hf–O isotopes of zircon in the Ahvenisto complex, southeastern Finland. J. Geol. Soc. 172 (1), 103–112. https://doi.org/10.1144/jgs2014-013.

IAEA, 2003. Extent of environmental contamination by naturally occurring radioactive material (NORM) and technological options for mitigation. In: Agency, I.A.E. (Ed.), Technical Reports Series. International Atomic Energy Agency, Vienna.

Jamieson, J.W., Hannington, M.D., Tivey, M.K., Hansteen, T.H., Williamson, N.M.B., Steward, M., Fietzke, J., Butterfield, D., Frische, M., Allen, L., Cousens, B., Langer, J., 2016. Precipitation and growth of barite within hydrothermal vent deposits from the Endeavour Segment, Juan de Fuca Ridge. Geochim. Cosmochim. Acta 173, 64–85. https://doi.org/10.1016/j.gca.2015.10.021.

Kim, J.S., Kwon, S.K., Sanchez, M., Cho, G.C., 2011. Geological storage of high level nuclear waste. KSCE J. Civ. Eng. 15, 721–737. https://doi.org/10.1007/s12205-011-0012-8.

Klinkenberg, M., Brandt, F., Breuer, W., Bosbach, D., 2014. Uptake of Ra during the recrystallization of barite: a microscopic and time of flight-secondary ion mass spectrometry study. Environ. Sci. Technol. 48, 6620–6627. https://doi.org/10.1021/es405502e.

Klinkenberg, M., Weber, J., Barthel, J., Vinograd, V., Poonoosamy, J., Kruth, M., Bosbach, D., Brandt, F., 2018. The solid solution–aqueous solution system (Sr,Ba,Ra)SO_4 + H_2O: a combined experimental and theoretical study of phase equilibria at Sr-rich compositions. Chem. Geol. 497, 1–17. https://doi.org/10.1016/j.chemgeo.2018.08.009.

Kowalski, P.M., Lange, S., Deissmann, G., Sun, M., Kvashnina, K.O., Baker, R., Kegler, P., Murphy, G., Bosbach, D., 2020. Modeling of nuclear waste forms: state-of-the-art and perspectives. MRS Advances 5, 213–222. https://doi.org/10.1557/adv.2020.38.

Kurniawan, T.A., Othman, M.H.D., Singh, D., Avtar, R., Hwang, G.H., Setiadi, T., Lo, W.-H., 2021. Technological solutions for long-term storage of partially used nuclear waste: a critical review. Ann. Nucl. Energy 166, 108736. https://doi.org/10.1016/j.anucene.2021.108736, 2021.

Kutzschbach, M., Glodny, J., 2024. LA-ICP-MS/MS-based Rb-Sr isotope mapping for geochronology. ChemRxiv. https://doi.org/10.1039/D3JA00297G.

Krauskopf, K.B., 1986. Thorium and rare-earth metals as analogs for actinide elements. Chem. Geol. 55, 323–335. https://doi.org/10.1016/0009-2541(86)90033-1.

Lange, S., Kowalski, P.M., Pšenička, M., Klinkenberg, M., Rohmen, S., Bosbach, D., Deissmann, G., 2018. Uptake of ^{226}Ra in cementitious systems: a complementary solution chemistry and atomistic simulation study. Appl. Geochem. 96, 204–216. https://doi.org/10.1016/j.apgeochem.2018.06.015.

Latimer, W.M., 1951. J. Am. Chem. Soc. 73, 1480–1482.

Manocchi, F.H., Campos, M.P., Dellamano, J.C., Silva, G.M., 2014. Radon exposure at a radioactive waste storage facility. J. Radiol. Prot. 34, 339. https://doi.org/10.1088/0952-4746/34/2/339.

Marcus, Y., 1991. Thermodynamics of solvation of ions. Part. 5. – gibbs free energy of hydration at 298.15 K. J. chem. Soc. Faraday. Trans. 87, 2995–2999. https://doi.org/10.1039/FT9918702995.

Mathurin, F.A., Aström, M.E., Laaksoharju, M., Kalinowski, B.E., Tullborg, E.-L., 2012. Effect of tunnel excavation on source and mixing of groundwater in a coastal granitoidic fracture network. Environ. Sci. Technol. 46, 12779–12786. https://doi.org/10.1021/es301722b.

Monkhorst, H.J., Pack, J.D., 1976. Special points for Brillouin- zone integrations. Phys. Rev. B 13, 5188. https://doi.org/10.1103/PhysRevB.13.5188.

Olszewska, W., Miśkiewicz, A., Zakrzewska-Kołtuniewicz, G., Lankof, L., Pająk, L., 2015. Multibarrier system preventing migration of radionuclides from radioactive waste repository. Nukleonika 60 (3), 557–563. https://doi.org/10.1515/nuka-2015-0103.

Perdew, J.P., Burke, K., Ernzerhof, M., 1996. Generalized gradient approximation made simple. Phys. Rev. Lett. 77, 3865. https://doi.org/10.1103/PhysRevLett.77.3865.

Pidchenko, I.N., Christensen, J.N., Kutzschbach, M., Ignatyev, K., Puigdomenech, I., Tullborg, E.L., Roberts, N., Rasbury, E.T., Northrup, P., Tappero, R., Kvashnia, K.O., Schäfer, T., Suzuki, Y., Drake, H., 2023. Deep anoxic aquifers could acta s sinks for uranium through microbial-assisted mineral trapping. Commun. Earth Environ. 4, 128. https://doi.org/10.1038/s43247-023-00767-9.

Prieto, M., Putnis, A., Fernandez-Diaz, L., 1993. Crystallization of solid solutions from aqueous solutions in a porous medium: zoning in (Ba,Sr)SO_4. Geol. Mag. 130 (3), 289–299.

Putnis, A., Fernandez-Diaz, L., Prieto, M., 1992. Experimentally produced oscillatory zoning in the (Ba,Sr)SO_4 solid solution. Nature 358, 743–745. https://doi.org/10.1038/358743a0.

Rajabzadeh, M.A., 2007. A fluid inclusion study of a large MVT barite-fluorite deposit: komshecheh, Central Iran. Iran. J. Sci.Technol. Trans. A 31, A1.

Reuschel, M., Melezhil, V.A., Whitehouse, M.J., Lepland, A., Fallick, A.E., Strauss, H., 2012. Isotopic evidence for a sizeable seawater sulfate reservoir at 2.1 Ga. Precambrian Res. 192–195, 78–88. https://doi.org/10.1016/j.precamres.2011.10.013.

Rosenberg, Y.O., Metz, V., Oren, Y., Volkman, Y., Ganro, J., 2011. Co-precipitation of radium in high ionic strength systems: 2. Kinetic and ionic strength effects. Geochim. Cosmochim. Acta 75, 5403–5422. https://doi.org/10.1016/j.gca.2011.07.013.

Rosenberg, Y.O., Metz, V., Ganor, J., 2013. Radium removal in a large scale evaporitic system. Geochem. Cosmochim. Acta 103, 121–137. https://doi.org/10.1016/j.gca.2012.10.046.

Rosenberg, Y.O., Sadeh, Y., Metz, V., Pina, C.M., Ganor, J., 2014. Nucleation and growth kinetics of $Ra_xBa_{1-x}SO_4$ solid solution in NaCl aqueous solutions. Geochim. Cosmochim. Acta 125, 290–307. https://doi.org/10.1016/j.gca.2013.09.041.

Seaborg, G.T., 1992. Overview of the actinide and lanthanide (the f) elements. Radiochim. Acta 61, 115–122. https://doi.org/10.1524/ract.1993.61.34.115.

Shock, E.L., Sassani, D.C., Willis, M., Sverjensky, D.A., 1997. Inorganic species in geologic fluids: correlations among standard molal thermodynamic properties of aqueous ions and hydroxide complexes. Geochem. Cosmochim. Acta 61, 907–950. https://doi.org/10.1016/S0016-7037(96)00339-0.

SKB Technical Report TR-21-07, 2022. Radionuclide Transport Report. PSAR version. ISSN 1404-0344.

Smith, D.W., 1977. Ionic hydration enthalpies. J. Chem. Educ. 54, 549. https://doi.org/10.1021/ed054p540.

Torapava, N., Ramebäck, H., Curti, E., Lagerkvist, P., Ekberg, C., 2014. Recrystallization of ^{223}Ra with barium sulfate. J. Radioanal. Nucl. Chem. 301, 545–553. https://doi.org/10.1007/s10967-014-3170-6.

Vanderbilt, D., 1990. Soft self-consistent pseudopotentials in a generalized eigenvalue formalism. Phys. Rev. B 41, 7892. https://journals.aps.org/prb/abstract/10.1103/PhysRevB.41.7892.

Vinograd, V.L., Kulik, D.A., Brandt, F., Klinkenberg, M., Weber, J., Winkler, B., Bosbach, D., 2018a. Thermodynamics of the solid solution - aqueous solution system $(Ba,Sr,Ra)SO_4 + H_2O$: I. The effect of strontium content on radium uptake by barite. Appl. Geochemistry 89, 59–74. https://doi.org/10.1016/j.apgeochem.2017.11.009.

Vinograd, V.L., Kulik, D.A., Brandt, F., Klinkenberg, M., Weber, J., Winkler, B., Bosbach, D., 2018b. Thermodynamics of the solid solution - aqueous solution system $(Ba,Sr,Ra)\ SO_4 + H_2O$: II. Radium retention in barite-type minerals at elevated temperatures. Appl. Geochemistry 93, 190–208. https://doi.org/10.1016/j.apgeochem.2017.10.019.

Vital, M., Daval, D., Morvan, G., Martinez, D.E., Heap, M.J., 2020. Barite growth rates as a function of crystallographic orientation, temperature, and solution saturation state. Cryst. Growth Des. 20, 3663–3672. https://doi.org/10.1021/acs.cgd.9b01506.

Wallin, B., 2011. Bacterial Sulphate Reduction and Mixing Processes at the Äspo Hard Rock Laboratory Indicated by Groundwater $d^{34}S$ Isotope Signatures. Swedish Nuclear Fuel and Waste Management Co. (SKB), Stockholm, Sweden. Report R- 11-13.

Weber, J., Barthel, J., Brandt, F., Klinkenberg, M., Breuer, U., Kruth, M., Bosbach, D., 2016. Nano-structural features of barite crystals observed by electron microscopy and atom probe tomography. Chem. Geol. 424, 51–59. https://doi.org/10.1016/j.chemgeo.2016.01.018.

Weber, J., Barthel, J., Klinkenberg, M., Bosbach, D., Breuer, U., Kruth, M., Brandt, F., 2017. Retention of ^{226}Ra by barite: the role of internal porosity. Chem. Geol. 466, 722–732. https://doi.org/10.1016/j.chemgeo.2017.07.021.

Weber, J., Bracco, J.N., Poplawsky, J.D., Ievlev, A.V., More, K.L., Lorenz, M., Bertagni, A. L., Jindra, S.A., Starchenko, V., Higgins, S.R., Stack, A.G., 2018. Unraveling the effects of strontium incorporation on barite growth - in situ and ex situ observations using multiscale chemical imaging. Cryst. Growth Des. https://doi.org/10.1021/acs.cgd.8b00839.

Whitehouse, M.J., 2013. Multiple sulfur isotope determination by SIMS: evaluation of reference sulfides for Δ33S with observations and a case study on the determination of Δ36S. Geostand. Geoanal. Res. 37 (1), 19–33. https://doi.org/10.1111/j.1751-908X.2012.00188.x.

Widanagamage, I.H., Schauble, E.A., Scher, H.D., Griffith, E.M., 2014. Stable strontium isotope fractionation in synthetic barite. Geochim. Cosmochim. Acta 147, 58–75. https://doi.org/10.1016/j.gca.2014.10.004.

Xiao, C., Fard, Z.H., Sarma, D., Sing, T.B., Xu, C., Kanatzidis, M.G., 2017. Highly efficient separation of trivalent minor actinides by a layered metal sulfide ($KInSn_2S_6$) from acidic radioactive waste. J. Am. Chem. Soc. 139 (46), 16494–16497. https://doi.org/10.1021/jacs.7b10464.

Yu, C., Drake, H., Lopez-Fernandez, M., Whitehouse, M., Dopson, M., Åström, M.E., 2019. Micro-scale isotopic variability of low-temperature pyrite in fractured crystalline bedrock—a large Fe isotope fractionation between Fe(II)aq/pyrite and absence of Fe-S isotope co-variation. Chem. Geol. 522, 192–207. https://doi.org/10.1016/j.chemgeo.2019.05.026.

Zhang, T., Gregory, K., Hammack, R.W., Vidic, R.D., 2014. Co-Precipitation of radium with barium and strontium sulfate and its impact on the fate of radium during treatment of produced water from unconventional gas extraction. Environ. Sci. Technol. 48, 4596–4603. https://doi.org/10.1021/es405168b.

Zielinski, R.A., Al-Hwaiti, M.S., Budahn, J.R., Ranville, J.F., 2010. Radionuclides, trace elements, and radium residente in phosphogypsum of Jordan. Environ. Geochem. Health 33 (2011), 149–165. https://doi.org/10.1007/s10653-010-9328-4.